# Modeling Ground-Shielded Integrated Inductors Incorporating Frequency-Dependent Effects and Considering Multiple Resonances

José Valdés-Rayón, Reydezel Torres-Torres, *Senior Member, IEEE*,
Roberto S. Murphy-Arteaga, *Senior Member, IEEE*,
and Germán Andrés Álvarez-Botero, *Member, IEEE*

***Abstract*— A model for integrated spiral inductors which incorporates the physically expected frequency-dependent effects modifying the device's impedance is proposed. Moreover, it is demonstrated that the effect of resonances occurring outside the bandwidth of applicability for the device may considerably influence the performance around the peak of the Q-factor versus frequency curve. In this paper, we present the use of cascaded resonant circuits to represent the additional resonances occurring in the device to improve model accuracy up to 60 GHz.**

***Index Terms*— Eddy current, ground shield, resonances, skin effect, spiral inductor.**

## I. Introduction

INDUCTORS are among the most important passive components used in radio frequency (RF) ICs [1]–[5]. In this regard, the quality ($Q$) factor is the typical figure of merit used to assess device performance [6]. However, this parameter strongly depends on the losses associated with eddy currents originated on the ground path. Thus, ground shields are used to avoid this effect at the highly lossy substrate level [1]–[7]. Generally, these shields use metal, polysilicon, or low-resistivity buried layers close to the silicon surface and may present either solid or patterned geometry [4], [5]. Bear in mind, however, that the electrical performance of the inductor is modified by the shield and thus needs to be considered in the corresponding model. For this purpose, equivalent circuits are used, most of them based on the $\pi$-model shown in Fig. 1(a) [8]–[15]. These models exhibit acceptable accuracy up to the frequency of occurrence of the inductor self-resonance. This frequency is referred to here as $f_{SRF1}$. The assumed topology for the $\pi$-model, however, requires that some elements take values without physical significance; especially, for those that present a large separation of the inductor from the ground shield ($h$). For instance, when assuming the topology in Fig. 1(a), the experimental data associated with the real part of the impedance between the input and output ports [i.e., Re($1/Y_f$)] exhibits negative values within certain frequency ranges, which would require considering negative resistances to represent $Y_f$. This effect is shown in Fig. 2 for inductors with different $h$ and different patterns for the shield: solid ground shield (SGS) and patterned ground shield (PGS). In order to overcome this problem, T-models as the one shown in Fig. 1(b) have been proposed [16]–[19].

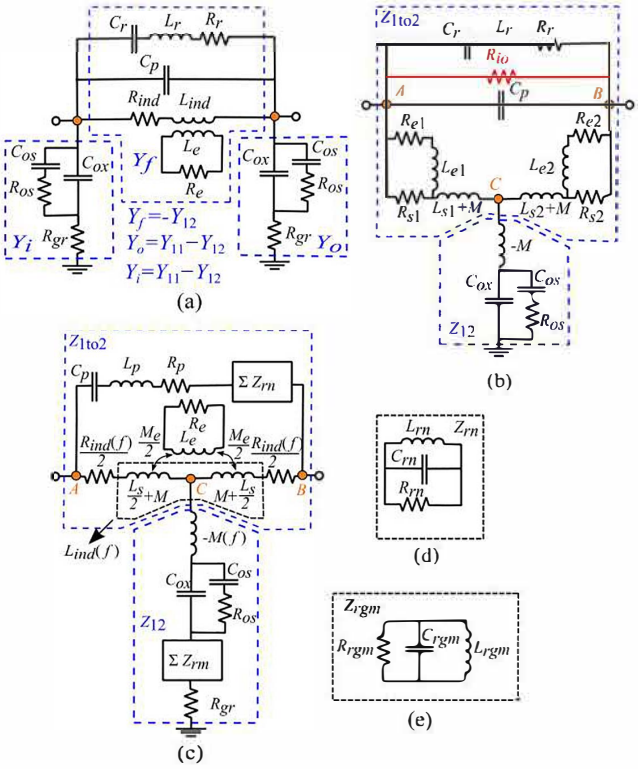


Fig. 1. Equivalent circuits for on-chip inductors. (a) $\pi$-model. (b) Conventional T-model. (c) Proposed T-model. (d) and (e) Subcircuits to represent higher order resonances.

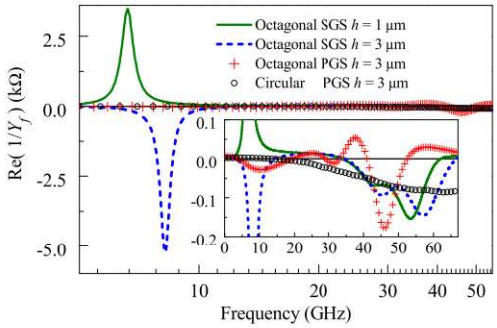


Fig. 2. $\mathrm{Re}(1/Y_f)$ curves obtained from data measured to different inductors when assuming the $\pi$-model representation. The fact that these curves exhibit negative value points out that the $\pi$-model does not allow for a physically based wideband representation of all inductor structures.

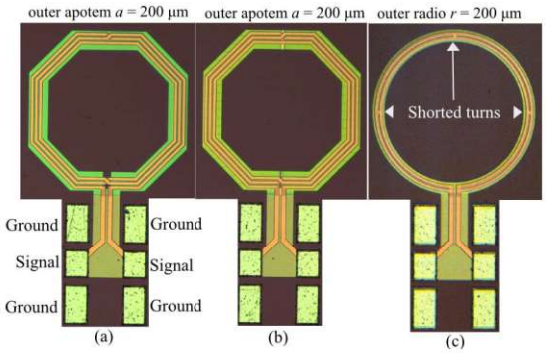


Fig. 3. Photographs of the fabricated inductors. (a) Octagonal with SGS. (Two devices presenting different separations from the shield were fabricated for this case.) (b) Octagonal with PGS. (c) Circular with PGS.

Nevertheless, these models include a resistance directly connecting the input and output ports ($R_{\mathrm{io}}$) that allow for the fitting of experiment with simulated data, but lacking physical meaning.

In this paper, we show that by accounting for the frequency dependence of the model elements representing the self-inductances and series resistances of the device, using $R_{\mathrm{io}}$ is avoided. This is achieved by employing the square root of frequency functions that describe the change in the current distribution within the cross section of the metal traces due to the skin effect. Conversely, to previous approaches [14], skin effect models relying on ladder equivalent circuits are not necessary, avoiding solving systems of nonlinear equations to extract the corresponding parameters.

Moreover, it is observed that resonances outside the frequency range around the fundamental inductor resonance may substantially influence the response within the bandwidth of applicability. This is due to the fact that a resonance is a wideband effect that gradually reduces its impact as the frequency of operation of the device moves away from the resonant frequencies. However, the effect of one or more of these resonances may not have completely vanished away within the frequency range of interest. In fact, in critical cases, even resonance overlapping may occur. Thus, properly considering multiple resonances allows representing device behavior for the desired frequencies in a physical manner. Here, the model topology for achieving this goal, as well as a systematic parameter extraction methodology, is provided and experimentally verified for inductors presenting different distances from the shield, different shield patterns, and octagonal and circular geometries. Excellent model–experimental correlation is achieved, correctly predicting the $Q$-factor.

## II. Prototypes and Measurements

To develop and verify this proposal, a test chip was fabricated in an RFCMOS process over a 20-Ω·cm resistivity p-type substrate. Micrographs of the fabricated inductors are shown in Fig. 3, while the corresponding dimensions are indicated in Fig. 4, and the experimental setup used to measure the devices is shown in Fig. 5.

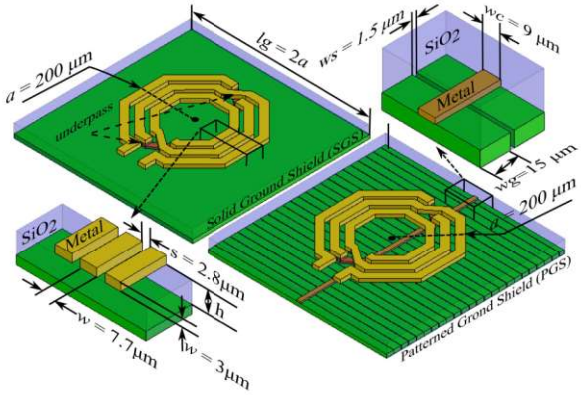


Fig. 4. Structure and dimensions for the octagonal inductors, which may present SGS or PGS. The structure for the circular inductor is the same.

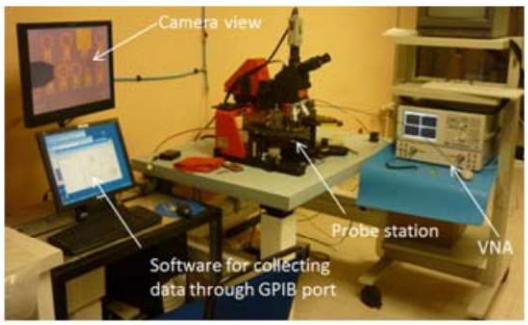


Fig. 5. Photograph of the experimental setup showing the probe station, the VNA, and the camera view with an image of the test chip.

All the fabricated devices are formed by copper traces with thickness $t = 3\ \mu$m and width $w = 7.7\ \mu$m and are isolated from the substrate by means of a shield at the lowest interconnection level made of polysilicon; as detailed as follows, this shield may be either solid (SGS) or patterned (PGS). The spacing between adjacent turns is $s = 2.8\ \mu$m, and the height between the metal trace and the ground shield is $h = 3.0\ \mu$m. The apothem of the outer turn for the three measured inductors is $a = 200\ \mu$m. Notice also in Fig. 3 that the inductors include aluminum coplanar pads, which are used to measure S-parameters using ground–signal–ground (GSG)

coplanar probes with a 100-$\mu$m pitch. Among these devices, three present octagonal geometry with three turns and exhibit the following characteristics: 1) one presents SGS and is separated from the shield a distance $h = 1$ $\mu$m; 2) a second one presents SGS and $h = 3$ $\mu$m; and 3) the third one presents PGS and $h = 3$ $\mu$m. A fourth inductor with circular geometry and two turns was fabricated presenting PGS, a radius of the outer turn of 200 $\mu$m, and $h = 3$ $\mu$m. As shown in Fig. 3(c), the turns of the circular inductor are joined by means of three small traces to increase the area for current flow. The analysis of this circular structure is also presented for comparison, and since circular inductors present a higher $Q$-factor [22].

The S-parameter measurements were performed using GSG coplanar probes presenting a 100-$\mu$m pitch. A VNA setup was calibrated up to the probe tips using an off-wafer line-reflect-match algorithm and an impedance standard substrate. In addition, the effect of the pads was de-embedded using measurements performed on on-wafer "open" and "short" dummy structures as described in [20]. Furthermore, since $Z$-parameters are used throughout the proposed methodology, the corresponding transformation from S-parameters was applied [21].

## III. Modeling and Parameter Extraction Methodology

The T-model proposed here includes two main impedance blocks enclosed in dashed boxes in Fig. 1(c); one associated with the impedance between ports 1 and 2 ($Z_{1to2}$), and the other accounting for the impedance that is common to ports 1 and 2 ($Z_{12}$). The subcircuits representing these impedances are discussed as follows. For the case of $Z_{1to2}$, there are two branches. The first one establishes the main path of current flows through the coil from port 1 to port 2 and includes the intrinsic inductance of the coil ($L_{\text{ind}}$) and the parasitic series resistance associated with the metal traces ($R_{\text{ind}}$). Notice that these elements exhibit frequency dependence due to the skin effect. Furthermore, an equivalent representation for the coupling between turns using a mutual inductance was presented in [16], and it is also used here. In addition, the impact of the eddy current loops occurring in the shield is represented with effective parameters: $L_e$, $R_e$, which are the eddy inductance and resistance, respectively, and $M_e$, which is the mutual inductance accounting for the magnetic coupling between the coil and the shield [9]–[17].

The second branch included in $Z_{1to2}$ represents the path originated by the capacitive coupling between the traces forming the turns. This path is due to current loops along the coil parallel to the shield and is represented by the series connection of the capacitor $C_p$, the inductor $L_p$, the resistor $R_p$, and the sum of the impedances $Z_{rn}$. For convenience during the development of the model, the impedance of this path, using $\omega$ for the angular frequency and $j^2 = -1$, is expressed as

$$Z_p = R_p + j\omega L_p - \frac{j}{\omega C_p} + \sum_{\forall n} Z_{rn} \qquad (1)$$

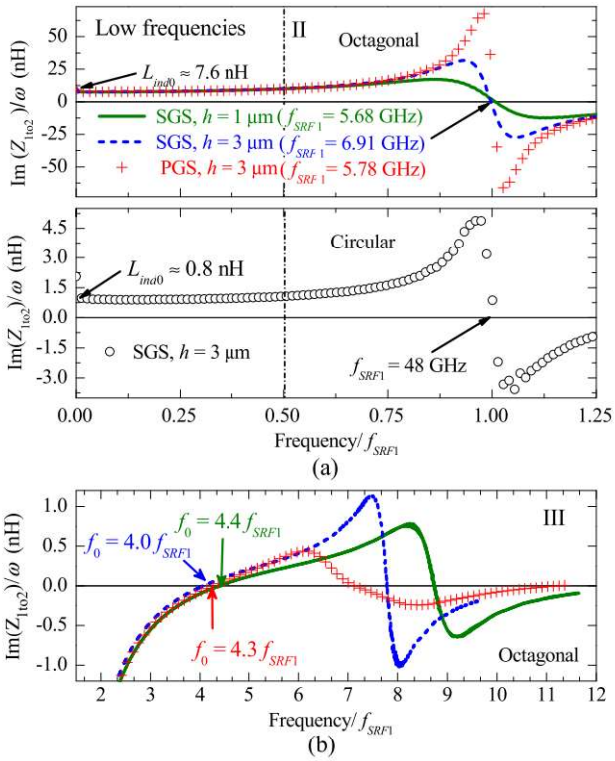


Fig. 6. Experimental curves of $\text{Im}(Z_{1to2})/\omega$ versus frequency normalized to $f_{\text{SFR1}}$ for (a) four measured inductors indicating the first two frequency ranges and (b) octagonal inductors showing multiple resonances in a third frequency range.

where the summation in the second term allows representing the resonances occurring in the device due to parasitic currents along the coil parallel to the ground shield.

On the other hand, the $Z_{12}$ block accounts for the parasitic current originated by the capacitive coupling between the coil and the shield. In this case, $C_{\text{ox}}$ is the capacitance to the ground shield, whereas $C_{\text{os}}$ and $R_{\text{os}}$ are related to fringing effects [13].

Notice that a series inductor given by $-M$ is included, which completes the equivalent representation of the mutual inductance between turns as explained in [16]. In addition, the sum of $Z_{rm}$ impedances allows accounting for the resonances occurring in the device due to parasitic current loops flowing through the coil and using the shield as return path [17], [18].

Now, in order to implement the model for a particular device, it is necessary to identify conditions at which the equivalent circuit can be simplified to ease parameter extraction in a systematic way. For this purpose, the experimental $\text{Im}(Z_{1to2})/\omega$ curves are plotted in Fig. 6(a) for all the inductors considered for this paper.

Notice that the frequency at which the inductor exhibits the first resonance (i.e., $f_{\text{SRF1}}$) can be read directly from these curves. Hence, it is reasonable to assume that frequencies $f \ll f_{\text{SRF1}}$ can be considered within a low frequency region since the effect of the inductor self-resonance is negligible. In this region, high-order effects such as those associated

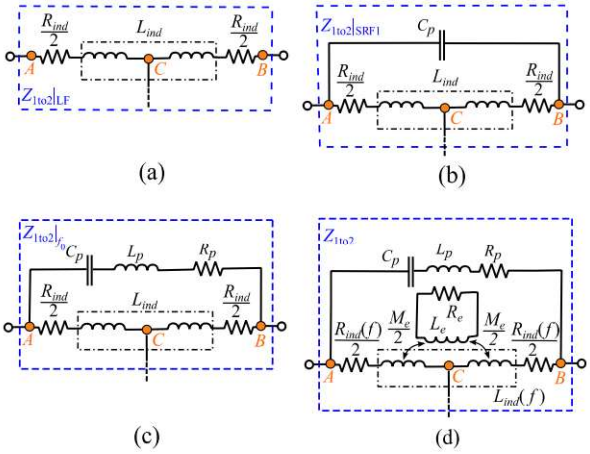


Fig. 7. Equivalent circuits of $Z_{1to2}$ under different frequency conditions. (a) Low frequencies. (b) At $f = f_{SRF1}$. (c) At $f = f_0$. (d) Wideband model.

with the impedances $Z_p$ and $Z_{1to2}$ can be ignored, and the equivalent circuit for the inductor is simplified to that shown in Fig. 7(a), which allows writing $Z_{1to2}$ as

$$Z_{1to2}|_{LF} \approx R_{ind0} + j\omega L_{ind0} \tag{2}$$

where $R_{ind0} \approx \mathrm{Re}(Z_{1to2}|_{LF})$ and $L_{ind0} \approx \mathrm{Im}(Z_{1to2}|_{LF})/\omega$ are the frequency-independent components of $R_{ind}$ and $L_{ind}$, respectively. Here, $Z_{1to2} = Z_{11} + Z_{22} - 2Z_{21}$ was obtained from the corresponding S-to-Z-parameter transformation.

Fig. 6(a) shows the values of $L_{ind0}$ for the four inductors considered, yielding approximately 7.6 nH for the octagonal inductors and 0.8 nH for the circular one. Interestingly, the three octagonal inductors yield approximately the same $L_{ind0}$ since the effect of the shield and the height of the inductor is not dominant at low frequencies. In addition, the extraction corresponding to $R_{ind0}$ is illustrated in Fig. 8(a), where it can be seen that the two octagonal inductors formed at the same metal level exhibit approximately the same resistance at low frequencies.

As the frequency increases from dc conditions, the effect of the first self-resonance is maximum at $f = f_{SRF1}$. Since, at this frequency, the combined effect of $L_{ind}$, $C_p$, and $R_{ind}$ is dominant and the skin effect is still not strong for the devices employed in current technologies, the equivalent circuit for $Z_{1to2}$ can be simplified to that shown in Fig. 7(b). Therefore, it is possible to write

$$f_{SRF1} \approx \frac{1}{2\pi\sqrt{L_{ind0}C_p}} \tag{3}$$

which can be solved for $C_p$ to obtain the corresponding value.

When the frequency increases beyond $f_{SRF1}$, a new resonance will become apparent; this is associated with the fact that a low impedance path will be established between ports 1 and 2. This occurs when the reactances associated with $C_p$ and $L_p$ cancel each other yielding $\mathrm{Im}(Z_{1to2}) = 0$. In Fig. 6(b), this effect is indicated for the octagonal inductors at $f = f_0$. Hence, similarly as for the previous resonance, for

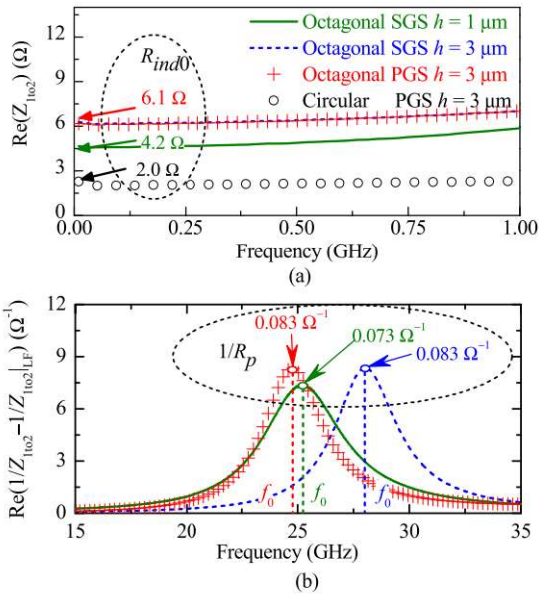


Fig. 8. Curves used to determine (a) $R_{ind0}$ and (b) $R_p$.

this one, it is possible to express

$$f_0 \approx \frac{1}{2\pi\sqrt{L_p C_p}} \tag{4}$$

which can be solved to obtain $L_p$ since $C_p$ is already known. Nevertheless, $R_p$ should also be considered as a loss contribution at $f = f_0$, and the equivalent circuit for the inductor at this condition is the one in Fig. 7(c). Therefore, once $L_{ind0}$, $R_{ind0}$, $L_p$, and $C_p$ have been determined, $R_p$ can be obtained from

$$\frac{1}{R_p} \approx \mathrm{Re}\left(\frac{1}{Z_{1to2}} - \frac{1}{R_{ind0} + j\omega L_{ind0}}\right)\Bigg|_{f=f_0} \tag{5}$$

where it is assumed that $L_{ind} \approx L_{ind0}$ and $R_{ind} \approx R_{ind0}$ at $f = f_0$. The corresponding extraction using (5) is shown in Fig. 8(b).

As frequency rises, the eddy currents become an important contribution modifying $Z_{1to2}$. A straightforward way to simplify the parameter extraction for the equivalent circuit is by shifting the effect of $L_e$, $R_e$, and $M_e$ in series with $L_{ind}$ and $R_{ind}$, by introducing an effective "eddy impedance" ($Z_{eddy}$) [10]. In this case, the experimental data associated with this impedance can be obtained by defining $k = M_e/(L_{ind}L_e)^{1/2}$ and $\tau = L_e/R_e$, which are the effective coupling coefficient and relaxation time associated with the eddy currents in the shield, respectively. Then

$$\left(Z_{1to2}^{-1} - Z_p^{-1}\right)^{-1} = R_{ind0} + j\omega L_{ind0} + \frac{\omega^2 L_{ind0} k\tau}{1 + j\omega\tau}. \tag{6}$$

The "eddy impedance" can be defined from this expression

$$Z_{eddy} \approx \left(Z_{1to2}^{-1} - Z_p^{-1}\right)^{-1} - (R_{ind0} + j\omega L_{ind0}). \tag{7}$$

Upon rearranging terms and considering only the real part of (7), a linear relation can be derived

$$\frac{\omega^2 L_{ind0}}{Re(Z_{eddy})} \approx \frac{\tau}{k}\omega^2 + \frac{1}{k\tau} \tag{8}$$

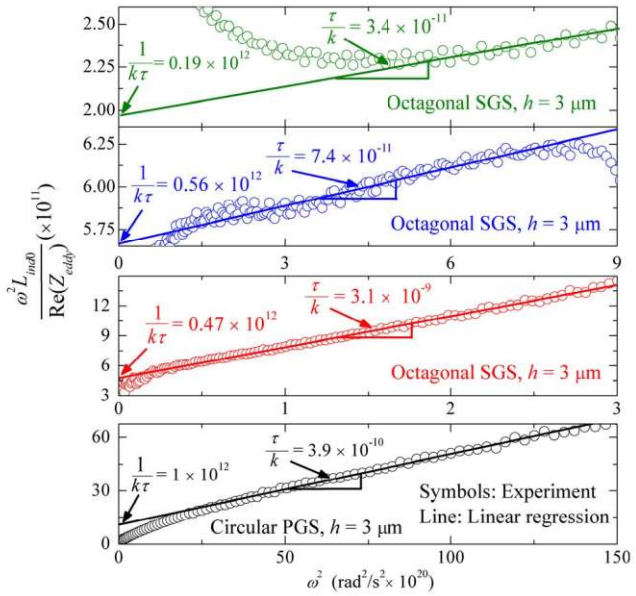


Fig. 9. Linear regressions to determine $k$ and $\tau$.

Clearly, $k$ and $\tau$ can be obtained from the slope and intercept with the $y$-axis of the linear regression for the experimental $\omega^2 L_{\text{ind0}}/\text{Re}(Z_{\text{eddy}})$ versus $\omega^2$ data; this is illustrated for the fabricated inductors in Fig. 9.

It is important to note that $R_{\text{ind}}$ and $L_{\text{ind}}$ have to be considered as frequency dependent beyond $f_{\text{SRF1}}$ to account for effects associated with the skin effect. In this case, $R_{\text{ind}}$ and $L_{\text{ind}}$ can be represented by [23]

$$L_{\text{ind}} = L_\infty + \frac{k_s}{2\pi\sqrt{f}} \tag{9}$$

$$R_{\text{ind}} = R_{\text{ind0}} + k_s\sqrt{f} \tag{10}$$

where $L_\infty$ is the inductance observed at high frequencies and $k_s$ is a constant parameter accounting for the proportionality of the impedance of a metal trace with the square root of frequency once the onset frequency for the skin effect has been surpassed. Multiplying (9) by the square root of frequency

$$L_{\text{ind}}\sqrt{f} = L_\infty\sqrt{f} + \frac{k_s}{2\pi} \tag{11}$$

which in terms of the experimental data can be written as

$$L_{\text{ind}}\sqrt{f} = \frac{\text{Im}\left[\left(Z_{\text{1to2}}^{-1} - Z_p^{-1}\right)^{-1}\right]}{2\pi\sqrt{f}}\left(1 - \frac{k\omega^2\tau^2}{1+\omega^2\tau^2}\right)^{-1}. \tag{12}$$

The parameters in (11) can be determined from a linear regression of (12), as shown in Fig. 10.

The final step in the parameter extraction is the representation of the higher order resonances, which is accomplished by using the model elements determined up to now, adding resonant circuits in series, as shown in Fig. 1(d). If we

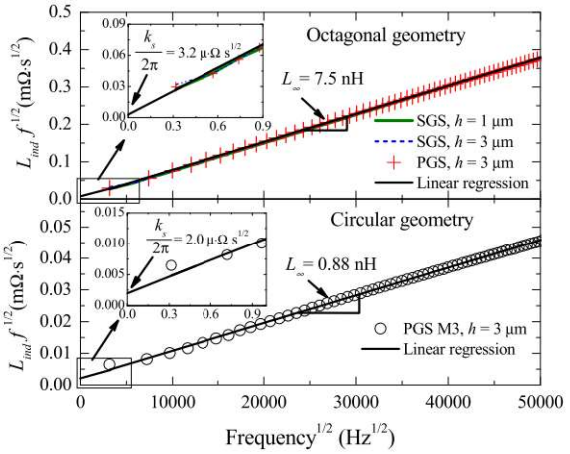


Fig. 10. Linear regressions used to determine $k_s$ and $L_{\text{ind0}}$.

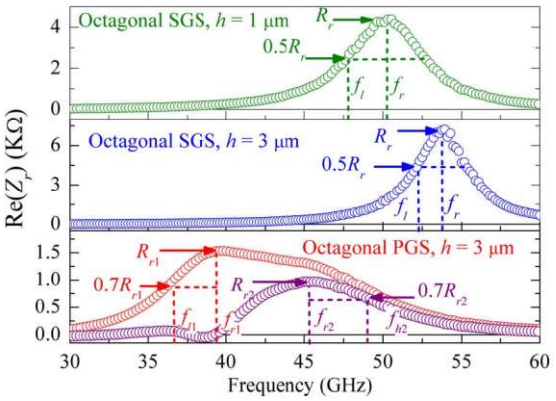


Fig. 11. Extraction of $f_r$, $f_h$, $f_l$, and $R_r$ from higher order resonances.

define [18]

$$Q_n = \frac{f_{rn}}{\text{BW}_n} \tag{13}$$

$$\text{BW}_n = f_{hn} - f_{ln} \tag{14}$$

$$L_{rn} = \frac{R_{rn}}{2\pi\, f_{rn}\, Q_n} \tag{15}$$

$$C_{rn} = \frac{Q_n}{2\pi\, f_{rn}\, R_{rn}} \tag{16}$$

where $f_{rn}$ is the frequency of the $n$th resonance and $f_{hn}$ and $f_{ln}$ are the values where the amplitude of the resonance is either 70% or 50%, depending on whether it is a simple resonance or a double overlap. The values of $f_{rn}$, $f_{hn}$, $f_{ln}$, and $R_{\text{rn}}$ can be obtained from the experimental data, as shown in Fig. 11. The corresponding values for the elements of Fig. 1(e) can be obtained from (13)–(16) using the correct subindexes.

Once all the elements of $Z_{\text{1to2}}$ have been determined, the elements of $Z_{12}$ can be extracted. However, it is necessary to de-embed the measurements in order to remove the effects of the intrinsic resonances of block $Z_{\text{1to2}}$ from $Z_{12}$. Blocks $Z_{\text{AC}}$, $Z_{\text{BC}}$, and $Z_{\text{AB}}$ are connected in a delta topology

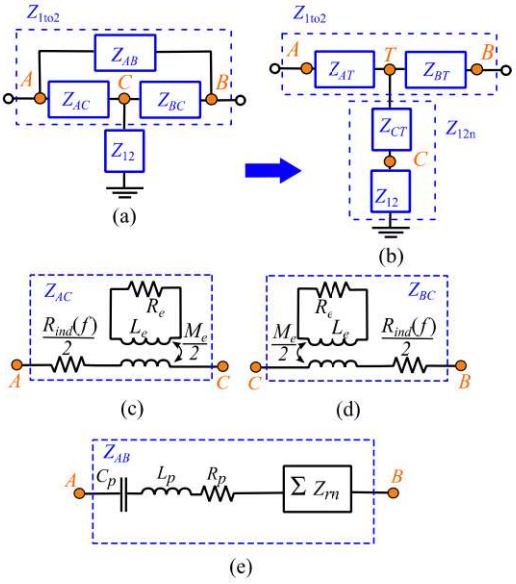


Fig. 12. Delta-to-star transformation used for the de-embedding process. (a) Block circuit for Fig. 1(c). (b) Star transformation of (a) to extract $Z_{12}$. (c) $Z_{AC}$ elements. (d) Elements of $Z_{BC}$. (e) Components of $Z_{AB}$.

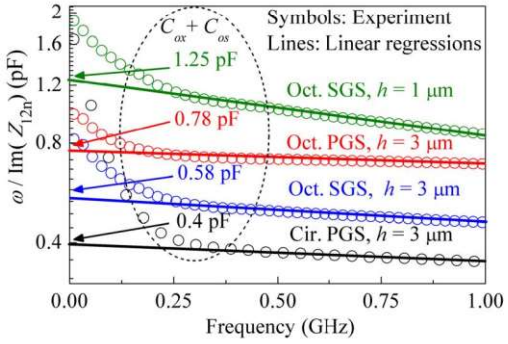


Fig. 13. Determination of $C_{ox} + C_{os}$ at low frequencies.

(see Fig. 12), which can be transformed into a star architecture using Kennelly's Theorem

$$Z_{CT} = \frac{Z_{AC}\, Z_{BC}}{Z_{AB} + Z_{BC} + Z_{AC}}. \tag{17}$$

The impedance block that is shown in Fig. 12(b) is defined as $Z_{12n} = Z_{12} + Z_{CT}$. Now, to find each one of the elements that constitute this impedance block, it is assumed that at very low frequencies the effects of $M(f)$ can be neglected and that $R_{gr}$ is in the order of a few ohms, which allows establishing [13]

$$-\frac{\omega}{\mathrm{Im}(Z_{12n}|_{\mathrm{LF}})}\bigg|_{\omega\to 0} = C_{os} + C_{ox}. \tag{18}$$

This relation is shown in Fig. 13.

Moreover, at low frequencies, it is possible to write the following relationship involving $R_{os}$ and $C_{os}$ [5]:

$$\omega^2 \mathrm{Re}(Z_{12n}|_{\mathrm{LF}})^{-1} = \frac{1}{R_{os} C_{os}^2} + \omega^2 R_{os}. \tag{19}$$

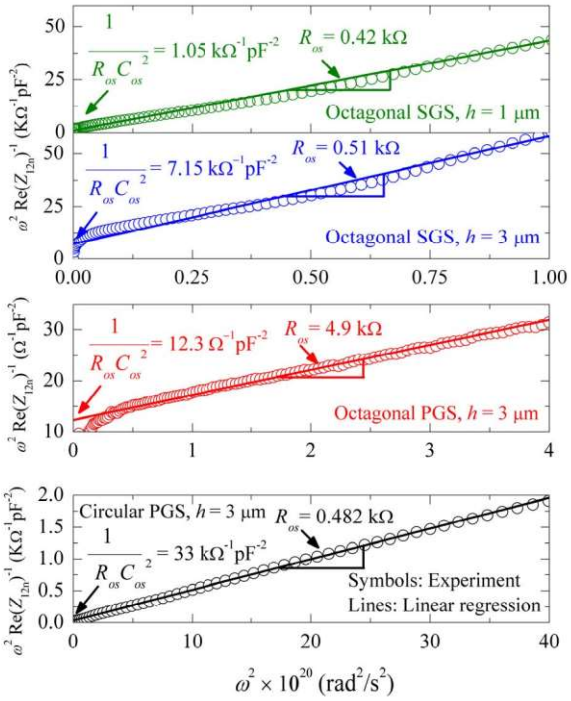


Fig. 14. Linear regressions used to determine $R_{os}$ and $C_{os}$ using low-frequency data.

Hence, $R_{os}$ and $C_{os}$ can be obtained from the slope and intercept with the $y$-axis of the linear regression for the experimental $\omega^2 \mathrm{Re}(Z_{12n})$ versus $\omega^2$ data at low frequencies; this is illustrated for the fabricated inductors in Fig. 14.

Furthermore, considering that $M$ is dependent on the effects of the intrinsic inductance of $Z_{1to2}$, it follows that it is also a function of frequency; therefore, skin effect and eddy current effects are included in this inductance, and hence, $M(f)$ can be directly defined as

$$M(f) = k_m L_{\mathrm{ind}} \left(1 + \frac{k\omega^2\tau}{1 + j\omega\tau}\right) \tag{20}$$

where $M_\infty$ is related to $L_\infty$ by

$$M_\infty = k_m L_\infty. \tag{21}$$

Here, $k_m$ is a constant factor, which relates mutual and intrinsic inductances. From the following equation, we can define

$$k_m = \frac{M_\infty}{L_\infty} \tag{22}$$

Therefore, the relationship between mutual and intrinsic inductances can be found using (21)–(23). A relation that allows the determination of $M_\infty$ from experimental data is herein proposed as

$$\frac{\mathrm{Im}[Z_{12n} - Z_{12n}|_{\mathrm{LF}}]}{\left(1 - \frac{k\tau^2\omega^2}{1+\tau^2\omega^2}\right)} \approx \omega\, M_\infty. \tag{23}$$

Clearly, (23) represents a line centered at the origin, $M_\infty$ being its slope, as can be seen in Fig. 15.

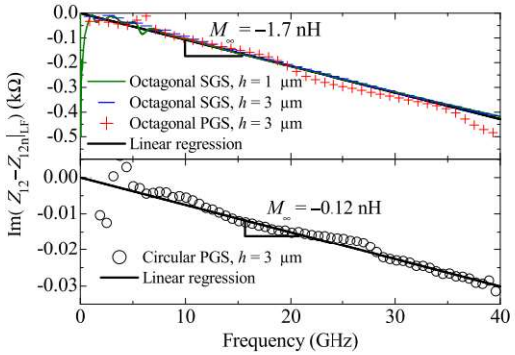


Fig. 15. Linear regression used to determine $M_\infty$ at high frequencies.

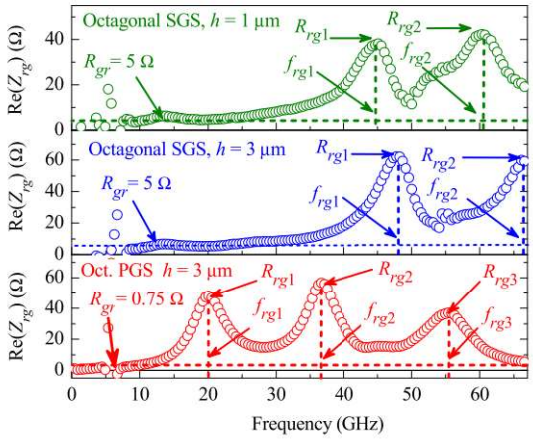


Fig. 16. Resonances in Re($Z_{12}$) for the octagonal inductors; as can be seen, for the PGS, a resonance is presented at 20 GHz, causing a reduction in the BW and in the efficiency of the inductor with this type of shield.

In all inductors, several resonances are present; to only extract the effects pertaining to these, it is necessary to apply the following equation on the experimental data:

$$Z_r = \mathrm{Re}[Z_{12n} - Z_{12n|\mathrm{LF}}] - M_\infty \left(\frac{k\omega^2\tau}{1+j\omega\tau}\right). \qquad (24)$$

The intrinsic effects of the resonances in each of the inductors are shown in Fig. 16. These resonances can be modeled using the parallel *RLC* resonant circuits defined in Fig. 1(c). These circuits are identical to those used for block $Z_{1to2}$; therefore, (13)–(16) can be used. The final experimental verification results are discussed in Section IV.

## IV. Results and Discussion

In order to point out the advantages of using the proposed model and parameter extraction methodology, the models shown in Fig. 1 were implemented in Keysight's ADS circuit simulator. Then, a comparison of $S_{11}$ and $S_{12}$ was performed for SGS and PGS structures. Notice, in Fig. 17, that the proposed model allows the modeling of these integrated inductors over a wide frequency range, including higher order resonances, independently of the ground shield used for the circuit design.

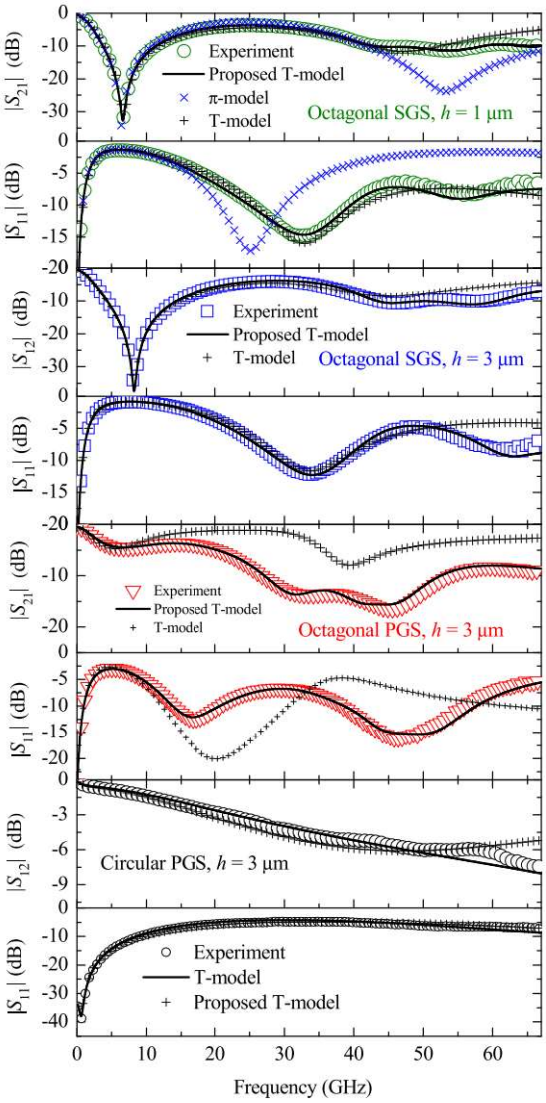


Fig. 17. Model–experimental correlations of S-parameters for the fabricated inductors.

It is important to remark that even though many circuit simulators which include frequency-dependent elements are readily available, the model for the higher order resonances in presented in this paper can be implemented in SPICE using arrays of frequency-independent elements, which is an advantage to improving integrated circuit design, evaluating process technology or optimizing device structure, since this model can be easily implemented in commercial circuit simulators.

In addition, as shown in Fig. 18, the $Q$-factor calculated as in [24] reduces in bandwidth for inductors built over the PGS. This improvement is mainly due to the reduction of eddy currents effects. Thus, PSG inductors are better for filter design, but if the bandwidth is not a restrictive parameter, SGSs can be used.

In addition, as can be seen at the top of Fig. 17, in the octagonal inductor with SGS and $h = 1$ $\mu$m, the resonances are present at frequencies higher than 40 GHz, for which the $\pi$ and T models cannot be used, as their comparisons show.

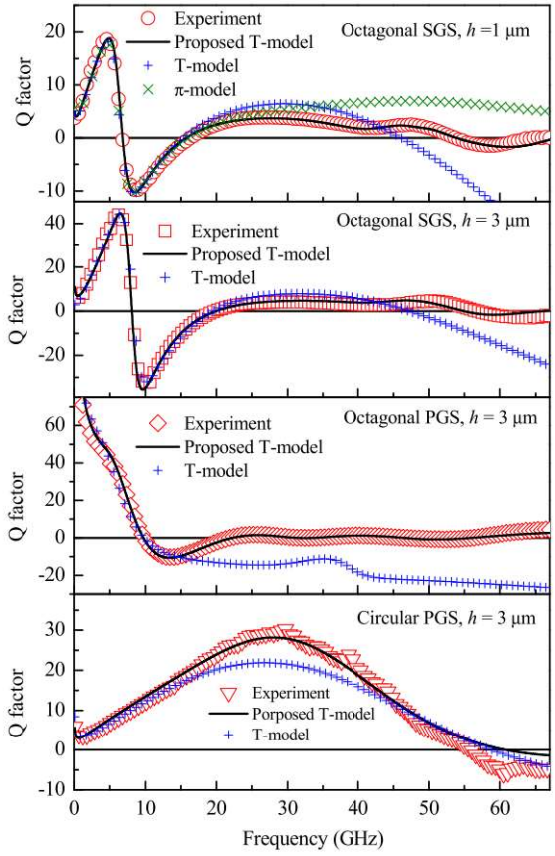


Fig. 18. Model–experimental correlations of $Q$-factor for the fabricated inductors.

TABLE I
COMPONENT VALUES OF THE EQUIVALENT CIRCUIT FOR THE SPIRAL INDUCTORS [FIG. 1(C)]

| Component | Inductor | | | |
|---|---|---|---|---|
| | Oct. SGS $h$ = 1 μm | Oct. SGS $h$ = 3 μm | Oct. PGS $h$ = 3 μm | Cir. PGS $h$ = 3 μm |
| $R_{ind0}$ (Ω) | 4.6 | 6.1 | 6.1 | 2.0 |
| $L_{ind0}$ (nH) | 7.56 | 7.64 | 7.60 | 0.88 |
| $L_{\infty}$ (nH) | 7.48 | 7.56 | 7.50 | 0.82 |
| $k_s$ ($10^{-6}$) | 2.81 | 2.35 | 3.22 | 2.00 |
| $C_p$ (fF) | 105 | 70 | 97 | 10 |
| $R_p$ (Ω) | 10.9 | 9.6 | 5.4 | 21 |
| $L_p$ (nH) | 0.15 | 0.22 | 0.17 | 0.27 |
| $k$ | 0.48 | 0.21 | 0.027 | 0.05 |
| $\tau$ ($10^{-11}$s) | 1.7 | 2.0 | 7.0 | 3.46 |
| $k_s$ (μΩ s$^{1/2}$) | 3.2 | 3.2 | 3.2 | 2.0 |
| $C_{ox}$ (fF) | 94 | 84 | 784 | 100 |
| $C_{os}$ (pF) | 1.5 | 0.52 | 0.01 | 0.39 |
| $R_{os}$ (kΩ) | 0.423 | 0.513 | 4.914 | 0.65 |
| $M_{\infty}$(nH) | -1.50 | -1.57 | -1.74 | -0.16 |
| $k_m$ | 0.21 | 0.23 | 0.24 | 0.19 |
| $R_{gr}$ (Ω) | 5.0 | 5.0 | 0.75 | 14 |

Moreover, for the octagonal inductor with SGS and $h = 3$ $\mu$m, the higher order resonances also appear at frequencies greater than 40 GHz; however, as explained earlier, the $\pi$-model cannot be used since it presents an anomalous behavior at the resonant frequency, and thus, our model is only compared to a previously published T-model. Furthermore, as can be seen in Fig. 17, for the octagonal inductor with PGS and $h = 3$ $\mu$m, higher order resonances are present from 20 GHz onward, and the conventional T model ceases to represent the structure for these higher frequencies. This is very important since most designs currently use inductors with PGSs and require being modeled over a broad BW, at least above the third harmonic, which in these cases would exceed 20 GHz. The model presented herein guarantees a good correlation even at higher frequencies. Finally, using a circular inductor, we have shown that this model can be applied to geometries other than the octagonal one, achieving excellent accuracy up to 60 GHz.

To summarize, the most important parameters for the model of each type of inductor are listed in Table I.

In any case, the excellent model–experimental correlation using the proposed equivalent-circuit model validates the extraction methodology and shows a suitable alternative for modeling on-chip inductors at microwave frequencies while simultaneously maintaining accuracy when different ground shields are used for the structures.

## V. CONCLUSION

The inclusion of frequency-dependent elements, as well as resonant circuits to take into account higher order resonances, translates into a versatile, yet simple, model for integrated circuit inductors. The proposed model correlates very well with experimental data obtained from inductors that have different ground shields, at different depths. This model makes it unnecessary to resort to artificial components (such as $R_{\rm io}$) that improve curve fitting but have no direct correspondence to the physical structure. Furthermore, proximity effects have been adequately included in the model, resulting in a true representation of the behavior in frequency of the fabricated structures.

## ACKNOWLEDGMENT

The authors would like to thank IMEC, Heverlee, Belgium, for supplying the test structures.

## REFERENCES

[1] P. Karjalainen, J. Rapelo, and E. O. Ristolainen, "The effects of metal ground shield on on-chip spiral inductors," *Phys. Scripta*, vol. T114, pp. 113–116, Jan. 2004.

[2] H.-B. Liang, Y.-S. Lin, C.-C. Chen, and J.-H. Lee, "Optimization of PGS pattern of transformers/inductors in standard RF BiCMOS technology for RFIC applications," in *Proc. IEEE Radio Freq. Integr. Circuits (RFIC) Symp.*, Jul. 2006, pp. 1–4.

[3] L. F. Tiemeijer, R. J. Havens, Y. Bouttement, and H. J. Pranger, "Physics-based wideband predictive compact model for inductors with high amounts of dummy metal fill," *IEEE Trans. Microw. Theory Techn.*, vol. 54, no. 8, pp. 3378–3386, Aug. 2006.

[4] Y.-S. Lin, C.-Z. Chen, H.-B. Liang, and C.-C. Chen, "High-performance on-chip transformers with partial polysilicon patterned ground shields (PGS)," *IEEE Trans. Electron Devices*, vol. 54, no. 1, pp. 157–160, Jan. 2007.

[5] W.-Y. Yin, "On-chip EMC issue: The implementation of patterned ground shields for silicon devices," in *Proc. 18th Int. Zurich Symp. Electromagn. Compat.*, Nov. 2007, pp. 9–12.

[6] J. L. González, X. Aragonés, M. Molina, B. Martineau, and D. Belot, "A comparison between grounded and floating shield inductors for mmW VCOs," in *Proc. (ESSCIRC)*, Sep. 2010, pp. 250–253.

[7] A. Ghannam, D. Bourrier, C. Viallon, J.-M. Boulay, G. Bouisse, and T. Parra, "High-Q SU8 based above-IC inductors for RF power devices," in *Proc. IEEE 11th Topical Meeting Silicon Monolithic Integr. Circuits RF Syst.*, Feb. 2011, pp. 25–28.

[8] R. Murphy-Arteaga, J. Huerta-Chua, A. Sánchez, A. Torres-Jacome, W. Calleja-Arriaga, and M. Landa-Vázquez, "Fabrication, characterisation and modelling of integrated on-silicon inductors," *Microelectron. Rel.*, vol. 43, no. 2, pp. 195–201, Feb. 2003.

[9] H. Zou, J. Liu, J. Wen, H. Wang, L. Sun, and Z. Yu, "A novel wideband 1-$\pi$ model with accurate substrate modeling for on-chip spiral inductors," in *Proc. IEEE Custom Integr. Circuits Conf.*, Nov. 2010, pp. 1–4.

[10] D. Pasquet, P. Descamps, D. Lesenechal, L. Nguyen-Tran, E. Bourdel, and S. Quintanel, "Modelling of an inductor on SiGe: From the measurement to the equivalent scheme," in *Proc. Microw., Radar Remote Sens. Symp.(MRRS)*, Oct. 2011, pp. 59–64.

[11] Y.-S. Tsai and T.-S. Horng, "Wideband compact PI equivalent circuit for modeling on-chip spiral inductors," *IEEE Microw. Wireless Compon. Lett.*, vol. 22, no. 1, pp. 26–28, Jan. 2012.

[12] N. Yan, C. Yang, and J. Gao, "An approach for determining equivalent circuit model of on-chip inductors," *Microw. Opt. Tech. Lett.*, vol. 55, no. 10, pp. 2363–2370, Oct. 2013.

[13] S. C. Sejas-García, R. Torres-Torres, and L. C. Moreira, "Systematic modeling and parameter extraction for on-chip inductors in CMOS technology," in *Proc. SBMO/IEEE MTT-S Int. Microw. Optoelectron. Conf.*, Aug. 2013, pp. 1–5.

[14] B. Han, Z. Tian, and D. Wang, "Analysis of scalable two-$\pi$ equivalent-circuit model for on-chip spiral inductors," *Int. J. RF Microw. Comp. Aid. Eng.*, vol. 25, no. 2, pp. 93–100, Feb. 2015.

[15] J. Valdés-Rayón, R. Torres-Torres, and R. S. Murphy-Arteaga, "Analytical model parameter determination for microwave on-chip inductors up to the second resonant frequency," in *Proc. Int. Caribbean Conf. Devices, Circuits Syst. (ICCDCS)*, Jun. 2017, pp. 25–28.

[16] G. Yang, Z. Wang, and K. Wang, "Modified T-model with an improved parameter extraction method for silicon-based spiral inductors," *IEEE Microw. Wireless Compon. Lett.*, vol. 24, no. 11, pp. 817–819, Nov. 2014.

[17] J.-W. Jeong *et al.*, "Modeling of T-model equivalent circuit for spiral inductors in 90 nm CMOS technology," in *Proc. IEEE Int. Conf. Microelec. Test Struct. (ICMTS)*, May 2015, pp. 33–36.

[18] H. Wang, L. Sun, J. Liu, H. Zou, Z. Yu, and J. Gao, "Transfer function analysis and broadband scalable model for on-chip spiral inductors," *IEEE Trans. Microw. Theory Techn.*, vol. 59, no. 7, pp. 1696–1708, Jul. 2011.

[19] B. Han, R. Yue, J. Li, X. Shi, and D. Wang, "Comparison of lumped-parameter circuit models for on-chip spiral inductors," in *Proc. Asia-Pacific Microw. Conf. (APMC)*, Dec. 2015, pp. 1–3.

[20] S. Sejas-Garcia and R. Torres-Torres, "Deembedding on-wafer S parameters: Is a one-step procedure enough," in *Proc. 17th IBERCHIP Workshop*, 2012, pp. 174–178.

[21] D. M. Pozar, *Microwave Engineering*, 4th ed. New York, NY, USA: Wiley, 2012, p. 192.

[22] C. Detcheverry *et al.*, "The effect of copper design rules on inductor performance," in *Proc. Eur. Solid-State Dev. Res. Conf. (ESSDERC)*, Sep. 2003, pp. 107–110.

[23] D. M. Cortés-Hernández, and R. Torres-Torres, "Modeling the frequency-dependent series parasitics of ground–signal–ground pads used to probe on-wafer microstrip-line-fed devices," *IEEE Trans. Microw. Theory Techn.*, vol. 65, no. 6, pp. 2085–2092, Feb. 2017.

[24] T.-S. Horng, K.-C. Peng, J.-K. Jau, and Y.-S. Tsai, "S-parameter formulation of quality factor for a spiral inductor in generalized two-port configuration," *IEEE Trans. Microw. Theory Techn.*, vol. 51, no. 11, pp. 2197–2202, Nov. 2003.